REVIEW ARTICLE

A review of algorithms and software for real-time electric field modeling techniques for transcranial magnetic stimulation

Tae Young Park[1,2,3] · Loraine Franke[4] · Steve Pieper[5] · Daniel Haehn[4] · Lipeng Ning[3,6]

Abstract

Transcranial magnetic stimulation (TMS) is a device-based neuromodulation technique increasingly used to treat brain diseases. Electric field (E-field) modeling is an important technique in several TMS clinical applications, including the precision stimulation of brain targets with accurate stimulation density for the treatment of mental disorders and the localization of brain function areas for neurosurgical planning. Classical methods for E-field modeling usually take a long computation time. Fast algorithms are usually developed with significantly lower spatial resolutions that reduce the prediction accuracy and limit their usage in real-time or near real-time TMS applications. This review paper discusses several modern algorithms for real-time or near real-time TMS E-field modeling and their advantages and limitations. The reviewed methods include techniques such as basis representation techniques and deep neural-network-based methods. This paper also provides a review of software tools that can integrate E-field modeling with navigated TMS, including a recent software for real-time navigated E-field mapping based on deep neural-network models.

Keywords Transcranial magnetic stimulation · Electric field modeling · Deep neural networks · Real-time prediction · Navigated TMS

1 Introduction

Transcranial magnetic stimulation (TMS) is a noninvasive neuromodulation technique that works by applying time-varying electric current to a magnetic coil to induce an electric field in the brain to modulate the underlying activity [1–3]. Repetitive TMS (rTMS) has been approved as a treatment for several brain diseases such as major depressive disorder (MDD) [4], obsessive-compulsive disorder (OCD) [5], migraine with aura [6], and smoking cessation [7]. A general hypothesis about the underlying mechanism is that TMS modulates disease-related brain pathways or neurocircuits by exciting or inhibiting the underlying neural activities [8], leading to improved behaviors or symptoms. Therefore, accurately localizing and modulating disease-related brain targets is critical to improving the treatment response. Several heuristic or data-driven brain targeting methods have been proposed based on neuroimaging data, including resting-state functional magnetic resonance imaging (MRI) [9–11] or diffusion MRI [12–14]. Thus, the computation of the optimal coil position that maximizes the stimulation of the selected brain targets is critical to improving the treatment response. In addition to its application for the treatment of mental diseases, TMS is often used as a tool to localize the brain function regions, such as brain cortex areas related to motor [15] or language [16] function, to improve the accuracy of neurosurgical planning for individual patients [17]. In these applications, accurate modeling of TMS-induced electric field (E-field) in brain tissue is important to optimize stimulation of selected brain targets related to mental diseases or localize brain function areas.

✉ Lipeng Ning
lning@bwh.harvard.edu

1 Bionics Research Center, Biomedical Research Division, Korea Institute of Science and Technology, Seoul 02792, Republic of Korea

2 Division of Biomedical Science and Technology, KIST School, Korea University of Science and Technology, Seoul 02792, Republic of Korea

3 Brigham and Women's Hospital, Boston, MA 02115, USA

4 University of Massachusetts Boston, Boston, MA 02125, USA

5 Isomics, Inc., Cambridge, MA 02138, USA

6 Harvard Medical School, Boston, MA 02115, USA

Accurate E-field modeling for individual subjects can significantly improve the treatment efficacy. E-field modeling usually involves techniques such as finite element modeling (FEM) and boundary element modeling (BEM) based on head models. These methods numerically solve the Maxwell equation to estimate the E-field induced by the time-varying magnetic field induced by the pulsed current in the TMS coil. Several specialized or general-purpose software has been used for TMS E-field modeling, including the open-source SimNIBS [18], commercial software SIM4LIFE [19], COMSOL Multiphysics [20], and other open-source algorithms [21]. These tools apply different E-field solvers to estimate the stimulation intensity on brain surfaces or volumes. The E-field hot spot at the brain surface provides valuable information about the underlying target engagement. Several methods have also been proposed to use the E-field intensity to determine the stimulation intensity for individual subjects accurately [22]. Furthermore, the direction of vector E-field is also potentially helpful in examining the relation between the orientation of the axon fiber bundles and tissue excitability [23].

E-field modeling techniques typically require creating complex tetrahedral mesh models of the head. The accuracy of the solution depends on the resolution of the head models [24]. Therefore, accurate E-field modeling typically requires high-resolution head models, which inevitably lead to long computation times. On the other hand, several TMS applications require fast or real-time E-field mapping for a moving coil during treatment. For example, rapid E-field mapping has been proposed to identify the network connections in the stimulated brain area [25]. Moreover, the real-time E-field mapping also provides more accurate information to determine the stimulation intensity for individual subjects. The stimulation dosimetry approach proposed in [22] requires the comparison of the E-field intensity in the target area and the intensity in the hand knob region related to the resting-state motor threshold during TMS experiments. Currently, the neuronavigation technique can accurately localize the position of a moving TMS coil relative to the head of the subject [26]. Navigated TMS is usually applied to a pre-defined brain target with a heuristic dosimetry approach. The long computation time of standard techniques is a major limitation for real-time navigated E-field modeling. Currently, to the best of our knowledge, the only commercial software for real-time E-field navigated TMS [15] uses a low-resolution solver based on over-simplified brain models [27], limiting the targeting accuracy in clinical applications. Therefore, there is a critical demand for fast or real-time E-field modeling techniques to provide timely feedback to optimize experimental parameters during the treatment.

The paper reviews several recent real-time or near real-time TMS E-field prediction techniques. We note that some

techniques are developed based on existing FEM [28, 29], BEM [30–32] and finite difference method (FDM) [33, 34], but with substantial further extensions to improve real-time applications. Interested readers are referred to the above references and this review paper [35] for more details about the underlying physics and algorithms. This paper will review several recent methods for real-time E-field prediction and related software for navigated TMS E-field mapping.

The organization of the paper is as follows. Section 2 provides an overview of fast E-field modeling techniques based on modified FEM methods. Section 3 provides a review of deep neural network-based methods and related software. Section 4 discusses the limitations of existing techniques and future directions.

2 Rapid E-field modeling methods

2.1 Basic concepts and equations

The E-field induced by a TMS coil is determined by the Maxwell–Faraday law of induction [36, 37]

$$\nabla \times \boldsymbol{E} = -\partial \boldsymbol{B}/\partial t, \tag{1}$$

where $\boldsymbol{B}$ and $\boldsymbol{E}$ denote the vector magnetic flux and electric field, respectively. The magnetic flux is divergence-free and can be represented by the curl of a vector magnetic potential as $\boldsymbol{B} = \nabla \times \boldsymbol{A}$. Therefore, Eq. (1) indicates that the E-field is represented as

$$\boldsymbol{E} = -\frac{\partial \boldsymbol{A}}{\partial t} - \nabla \phi, \tag{2}$$

where ϕ is a scalar potential function. Let $\boldsymbol{E}_p = -\frac{\partial \boldsymbol{A}}{\partial t}$, usually referred to as the primary or incident E-field determined by the coil shape and positions. The second term $-\nabla \phi$ is the secondary field, i.e., $\boldsymbol{E}_s = -\nabla \phi$, the primary variable to be estimated in E-field modeling. Therefore, the total E-field can be decomposed as $\boldsymbol{E} = \boldsymbol{E}_p + \boldsymbol{E}_s$.

The divergence of the induced current in the tissue is zero since there is no net current source within the tissue, which leads to the following equation

$$\nabla \cdot (\sigma \boldsymbol{E}) = \nabla \cdot \left(-\sigma \frac{\partial \boldsymbol{A}}{\partial t} - \sigma \nabla \phi \right) = 0, \tag{3}$$

where σ denotes the conductivity of the tissue. The conductivity is usually considered scalar-valued but can also be tensor-valued [18, 38]. Since there is no current injected or extracted at the skin surface, the E-field also satisfies the following boundary condition

$$\left(\sigma \frac{\partial \boldsymbol{A}}{\partial t} + \sigma \nabla \phi \right) \cdot \boldsymbol{n} = 0, \tag{4}$$

Fig. 1 Schematic diagram of TMS simulation. In this figure, the vector fields (i.e., $\frac{\partial A}{\partial t}$ and E) indicate its magnitude
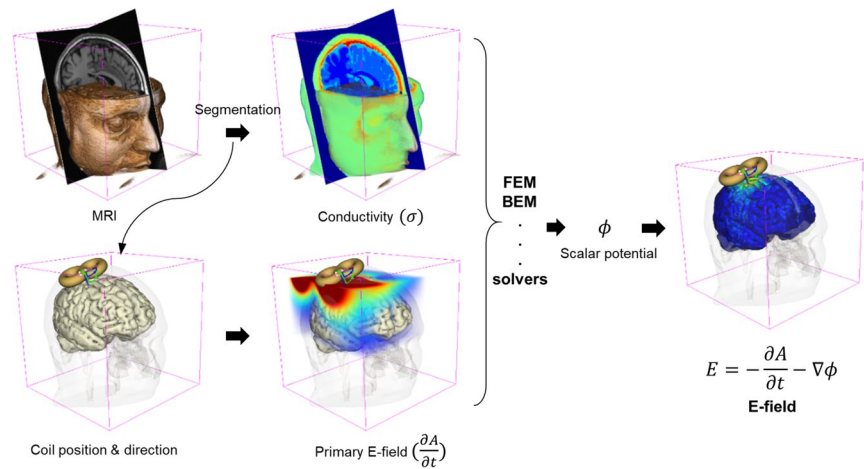
for any normal vector $\boldsymbol{n}$ on the surface.

Figure 1 illustrates the standard workflow for E-field molding, including the tissue segmentation based on MRI data, the creation of a tetrahedral mesh model of the head, sampling the primary E-field vector at the expected coil position, and applying the E-field solvers, such as FEM, BEM, to solve the E-field vector in the mesh space. Further processing steps are usually needed to sample the E-field vector to brain volume or surface for visualization and quantitative analysis. The creation of head models typically takes several hours of processing time. The E-field solvers usually take tens of seconds to several minutes to compute the E-field at one coil position. As is typical with all simulation studies, there is a trade-off between computation time and prediction accuracy [39]. Fast E-field prediction can be achieved using a simplified head model. For example, a fast BEM method was proposed in [40] to accelerate the prediction of E-field for head models by using separated computations of coil-dependent and -independent components and an approximation of integral algorithm. This approach can speed up the prediction time to about 27 coil positions per second, i.e., 37 ms per position, for a model with 5 tissue components, 50,000 vertices, 3-mm triangle-side length, and 9000 field points on the cortex. In general, the prediction time scales linearly with the number of field points.

The performance of the fast BEM in [40] was evaluated using reference results based on a 5-component model with 2.5-mm resolution using relative error (RE)

$$\text{RE} = \frac{|\boldsymbol{E}_{\text{ref}} - \boldsymbol{E}_{\text{pred}}|}{|\boldsymbol{E}_{\text{ref}}|}, \tag{5}$$

the correlation error (CCE)

$$\text{CCE} = 1 - \frac{(\boldsymbol{E}_{\text{ref}} - \overline{\boldsymbol{E}_{\text{ref}}}) \cdot (\boldsymbol{E}_{\text{pred}} - \overline{\boldsymbol{E}_{\text{pred}}})}{|\boldsymbol{E}_{\text{ref}} - \overline{\boldsymbol{E}_{\text{ref}}}||\boldsymbol{E}_{\text{pred}} - \overline{\boldsymbol{E}_{\text{pred}}}|}, \tag{6}$$

and relative magnitude (MAG)

$$\text{MAG} = \frac{|\boldsymbol{E}_{\text{pred}}|}{|\boldsymbol{E}_{\text{ref}}|}, \tag{7}$$

where $\boldsymbol{E}_{\text{ref}}$ and $\boldsymbol{E}_{\text{pred}}$ denote the reference and predicted vector E-field. The fast-BEM with 3-mm resolution provides $\text{RE} = 4.7\%, \text{CCE} = 0.1, \text{MAG} = 99.9\%$. However, the 3-mm resolution is lower than the resolution for standard FEM methods. The accuracy of BEM methods degrades significantly with the reduction of resolutions [39, 41]. Since the number of field points scales as a cube function of the spatial resolution, increasing the spatial resolution can significantly lengthen the computation time making classical techniques quickly become impractical. While advanced computation hardware can improve the computational performance of classical algorithms, there is a critical demand for new computation techniques to significantly accelerate the TMS E-field modeling.

To this end, several novel computation techniques have been developed to translate E-field modeling to real-time TMS applications. A summary of the fast E-field prediction algorithms is listed in Table 1. These techniques will be reviewed in the following two sections and classified into two groups based on the underlying principles.

2.2 Basis representation methods

Equation (3) indicates that the secondary E-field $\boldsymbol{E}_s$ is a linear function of the primary E-field $\boldsymbol{E}_p$. The linear relationship is utilized by a group of methods [42–44] to accelerate E-field mapping based on the basis representation techniques, as illustrated in Fig. 2. Assume that the primary E-field of a moving coil can be represented by a set of basis functions, i.e.,

Table 1 Summary of fast E-field prediction methods and performance

	Description	Parameters	Performance
Stenroos and Koponen [40]	Fast BEM; separated computations to coil-dependent and -independent parts	5 Components with 3 mm resolution; 42-dipole coil; reference model with 2-mm resolution	37 ms/position (GPU); RE = $4.2 - 5.2\%$, CC = $98.1 - 99.1\%$
Daneshzand et al. [42]	Basis representation; bipole-based MSP method	1500–3000 Dipoles, 5.5–18 h training time	100 ms/position (CPU), CC > 0.98, RE = $5 - 17\%$, RME = $5.1 - 5.7\%$
Wang et al. [43]	Basis representation; ACA-ADM method for low-rank basis learning	4 h training with 100-mm ROI, 14.3–18.7 h whole-brain	0.336–0.443 s/position (CPU); 6.6–8.5 ms/position (GPU); RE $< 2\%$
Hasan et al. [44]	Basis representation; PMD for learning group-level basis	9.5 h pre-processing per subject	0.57–0.85 s/position (CPU), 1.98–6.4 ms/position (GPU), RE $< 2\%$
Hasan et al.[41]	Basis representation; orthonormal mode decomposition	38 h pre-processing; analytic solutions for coefficients	1.2 s/position (CPU), 4 ms/position (GPU), RE $< 2\%$
Yokota et al. [45]	DNN; supervised learning, 3D-UNet	$72 \times 144 \times 24$ scalar E-field, coil-specific DNN	24 ms/position (GPU), MAD = 4.45%
Xu et al. [46]	DNN; supervised learning, modified 3D-ResUNet	$180 \times 220 \times 120 \times 3$ vector E-field, coil-specific DNN	24 s per position (GPU), CC = 0.997, MRE = 7.7%, Dist = 1.34 mm
Li et al. [47]	DNN; self-supervised learning, 3D U-Net	$208 \times 288 \times 304$ scalar E-field, evaluated at the DLPFC	1.4 s/position (GPU), RE = 1.2% mm, CC = 0.98, RME = 5.5%
Franke et al. [48]	DNN; the same model as in [46]	$70 \times 90 \times 50$ vector E-field; trained with multiple coils	15 ms/ position (GPU), CC = 0.9941, RE = 5.25%, RME = 2.89%, Dist = 1.05 mm

Fig. 2 An illustration of the basis-representation approach for E-field prediction. In this figure, the vector fields (i.e., $\frac{\partial A}{\partial t}$ and E) indicate its magnitude
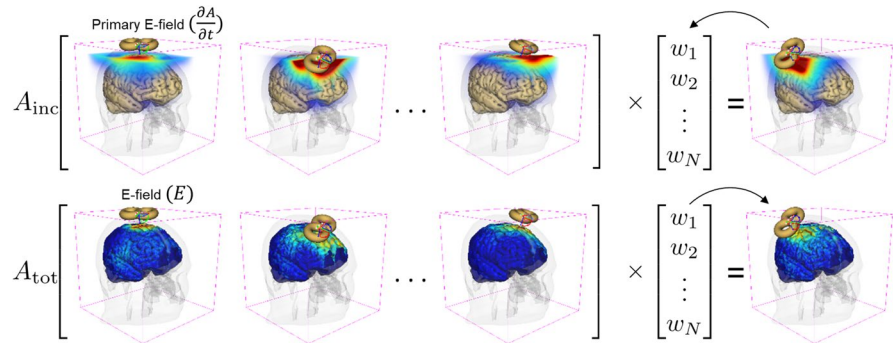
$$E_p = \sum_{n=1}^{N} w_n E_{p,n} = A_{\text{inc}} w, \qquad (8)$$

where $E_{p,n}$ represents a basic incident E-field component of the basis matrix $A_{\text{inc}} := [E_{p,1}, E_{p,2}, \ldots, E_{p,N}]$ with the corresponding total E-field being $E_{t,n}$. Then, the total E-field generated by a moving coil is equal to

$$E = \sum_{n=1}^{N} w_n E_{t,n} = A_{\text{tot}} w, \qquad (9)$$

where $A_{\text{tot}} := [E_{t,1}, E_{t,2}, \ldots, E_{t,N}]$. If all the $E_{t,n}$'s of the basis matrix A_{tot} are computed offline before the experiment, then the total E-field of a moving coil can be computed by using simple matrix multiplications. However, the computation methods vary in the choices of primary E-field basis matrices using dipoles or could and in learning algorithms of the A_{tot} basis matrices.

2.2.1 Magnetic stimulation profile (MSP) method

The Magnetic Stimulation Profile (MSP) method in [42] constructs the A_{inc} basis matrix using stationary dipoles, instead of TMS coils, placed at a fixed set of positions (1500–3000 dipoles) around the head model. Then, the total E-field for each basis field in A_{inc} is computed to create a new basis matrix A_{tot} using the fast multilevel multiple-based BEM method (BEM-FMM) [21]. Next, the representation coefficients w corresponding to the primary field of a moving coil are estimated using a regularized minimum-norm method as

$$w = \left(A_{\text{inc}}^T A_{\text{inc}} + \lambda^2 I \right)^{-1} A_{\text{inc}}^T E_p. \qquad (10)$$

where λ is the regularization parameter which was set to the highest singular value in the A_{inc}. Then, the predicted E-field (E) is given by $A_{\text{tot}} w$.

The MSP method took approximately 18 h to learn an A_{tot} basis matrix with a set of 3000 dipoles. The computation time was reduced to 5.5 h using only 1500 dipoles. Once the basis is learned, it only took 100 ms to predict the E-field on a mesh with 60,000 facets and 1500 dipoles.

The RE metric as in Eq. (5) was used in [42] to evaluate the performance of the algorithm. Other metrics include the correlation coefficient (CC), defined as CC = 1 − CCE for CCE defined in Eq. (6), and the relative maximum error (RME)

$$RME = \frac{\left| E_{ref}^{N} - E_{pred}^{N} \right|}{\left| E_{ref}^{N} \right|}, \tag{11}$$

where E_{ref}^{N} represents the N highest values of E_{ref}. The RME metric may provide more useful information for adjusting the stimulation intensity than the RE metric. For the MSP method using basis functions with 3000 and 1500 dipoles, the CC was > 0.98, with an RE ranging of 5–15% and an RME (with N = 10) of 5.1–5.7%.

2.2.2 Low-rank matrix approximation methods

The adaptive cross approximation and auxiliary dipole (ACA–ADM) method introduced in [43] is also based on the linear representations in Eqs. (8) and (9). However, there are several key differences compared to the MSP method. First, the ACA–ADM method uses the primary E-field of the TMS coil instead of dipoles at different locations to build the A_{inc} basis matrix. Second, the basis matrices in ACA–ADM have support on a finite set of tetrahedron regions of interest (ROI). Third, the ACA–ADM method uses a time-efficient approach to learn the basis function by utilizing the property that the basis matrix is essentially low-rank [49, 50].

The efficient basis learning approach is achieved by using the adaptive cross-approximation (ACA) algorithm [51–53]. Consider a basis matrix A_{tot} of size $N_t \times N_c$ where each column represents the total E-field in N_t tetrahedrons at one coil position. Then, the ACA algorithm recursively updates A_{tot} using a sequence of rank-1 updates where the value at the k-th iteration is represented by

$$A_{tot}^{(k)} = U^{(k)} V^{(k)}. \tag{12}$$

The size of $U^{(k)}$ is $3N_t \times k$ where N_t is the total number of tetrahedrons. $V^{(k)}$ is of size $k \times N_c$ where N_c denotes the total number of coil positions and orientations.

Each iteration of the ACA algorithm updates the columns of $U^{(k)}$ and the rows of $V^{(k)}$ using a Gram–Schmidt procedure [54] based on measures from one column and one row of A_{tot}. The column component represents the total E-field at one coil position, which is estimated by using the FEM method in [39]. Each row component represents the E-field

in a fixed ROI tetrahedron along one direction with different coil positions. The row entries can be computed using the auxiliary dipole method (ADM) [55], a fast algorithm to compute the average E-field in a brain ROI without computing the whole-brain E-field.

It was shown in [43] that the ACA–ADM method can significantly reduce the training time for small ROIs without reducing the prediction accuracy. For a small ROI with a 20-mm diameter and 6163×360 coil positions, the ACA–ADM approach only requires 17 iterations. The processing time for basis learning scales linearly with the rank of the matrix and approximately linearly with the size of the ROI. The ACA–ADM method takes 4 h of pre-processing for a 100 mm diameter ROI and can determine the ROI E-field with a 2% approximation error. Once the basis is learned, it takes 40 ms to compute the E-field in an ROI with a diameter less than 100 mm.

For a whole-brain ROI with 7.69–9.32 million coil placements, the processing time is between 14.3 and 18.7 h with a 2% accuracy. The computation time to reconstruct the whole brain E-field is 0.336–0443 s (CPU) and 6.6–8.5 ms (GPU).

2.2.3 Probability low-rank matrix approximation method

A general limitation of the MSP and ACA–ADM methods is that the basis matrix needs to be learned for the individual subject. The long processing time (> 10 h) is a limitation to predicting E-field for individual subjects for rTMS treatments. To avoid long processing time, [44] proposed an approach to prediction E-field maps in the group average brain. Thus, [44] proposed an approach to estimate a basis matrix $\bar{A}_{tot}$ where each column of the matrix represents the total E-field over the set of tetrahedrons at a fixed coil position averaged over a group of subjects. The $\bar{A}_{tot}$ only needs to be learned once. Then, it can be applied to predict the group average E-field map of a moving coil in real-time.

The probabilistic matrix decomposition (PMD) method was used in [44] for learning a low-rank approximation of the $\bar{A}_{tot}$ matrix. In the PMD method, a rank-k approximation of $\bar{A}_{tot}$ of size $N_t \times N_c$ is defined as

$$\bar{A}_{tot} = QB \tag{13}$$

where Q is of size $N_t \times k$ whose columns form an orthonormal basis to approximate the subspace spanned by the first left singular vectors of $\bar{A}_{tot}$, and B is of size $k \times N$, where N_t denotes the number of tetrahedrons in the target ROI.

In the PMD method, a Gaussian random Ω of size $N_c \times k$ is first generated to compute the matrix

$$Y = \bar{A}_{tot}\Omega, \tag{14}$$

where each column represents the total E-field of a random combination of coils. Since $\bar{A}_{tot}$ is unknown, Y can not be

computed directly using matrix multiplications. Instead, each column of Y is directly computed by using the FEM method with the primary E-field given by each column of the matrix $A_{\text{inc}}\Omega$. For a group of N_s subjects, a total number of $N_s \times k$ FEM steps is required. Once the matrix Q is obtained, the matrix B is given by $B = Q^T \bar{A}_{\text{tot}}$. Since $\bar{A}_{\text{tot}}$ is unknown, each row of B is computed by applying ADM to a linear combination of tetrahedron ROIs based on each row of Q^T.

The computation complexity of the PMD method is similar to the ACA–ADM method, with 9.5 h of processing time per subject with a rank of $k = 110$ for an approximation error of 2%. An advantage of the PMD method is that a theoretical bound exists to guide the choice of low-rank approximation. Once the basis is learned, the E-field can be predicted in almost real-time with 50–60 ms on a brain surface with 25,000 vertices. However, the results in [44] also showed significant inter-subject variability across different brain regions in the E-field.

2.2.4 Orthonormal mode decomposition method

In the basis-representation method, the expansion coefficient w is usually computed using the regularized minimum-norm method as in Eq. (10). This method requires large computer memory for a large set of densely sampled coil positions, which can slow down the computation speed. To overcome the limitation, [41] introduced an algorithm that provides analytical solutions of the representation coefficients using a set of orthonormal mode functions of the E-field maps.

For the method in [41], a set of N_m total E-field was first computed using the FEM method based on a set of randomly generated magnetic currents which are denoted by $E_W^{(1)}, E_W^{(2)}, \ldots, E_W^{(N_m)}$. Then, the singular value decomposition (SVD) was applied to decompose the E-field into a set of orthonormal mode functions $M^{(1)}, M^{(2)}, \ldots, M^{(N_m)}$. The total E-field of a moving coil is approximated by

$$E^{(N_m)} = \sum_{k=1}^{N_s} w_k M^{(k)} \tag{15}$$

with the representation coefficients estimated to minimize the L_2 error $\|E - E^{(N_m)}\|$.

Since $M^{(1)}, \ldots, M^{(N_s)}$ are orthonormal functions, the optimal representation coefficient w_k is given by

$$w_k = \langle M^{(k)}, E \rangle := \int_V M^{(k)} \cdot E dv, \tag{16}$$

where V represents the whole-brain volume. Since E is unknown, [41] proposed an approach to use reciprocity and Huygen's equivalence principles to compute the w_k as

$$w_k = \int_S \left[E_p \cdot J_S^{(k)} - H_p \cdot K_S^{(k)} \right] ds, \tag{17}$$

where S represents the Huygens' surface and E_p, H_p represents the primary E-field and H-field, $J_S^{(k)}$ and $K_S^{(k)}$ are equivalent surface currents associated with the k-th mode function, see [41] for more details.

The performance of the orthonormal basis approach was evaluated using a varying number of modes from 100 to 500 for different types of coils. The global vector error (GVE), global magnitude error (GME), local vector error (LVE), and local magnitude error (LME) were used to evaluate the performance of the algorithms. The GVE and LVE were the same as the RE and RME metrics defined above. The GME and LME are defined similarly to RE and RME based on the magnitude of the E-field maps. The algorithm in [41] requires more than 325, 425 and 375 mode functions for Fig. 8, D-B80, and Cool-40 coils to achieve a GME below 2% using head models generated by *mri2mesh* from Sim-NIBS. Reducing GVE below 2% requires more than 450, 550 and 375 mode functions for Fig. 8, D-B80, and Cool-40 coils. On average, the pre-processing time required to generate 400 modes is about 38 h. Once the mode functions are computed, the total computation time is less than 2.5 ms in GPU and less than 1.6 s in CPU with 500 mode functions.

2.3 Deep-learning based E-field prediction

Deep neural networks (DNNs) have revolutionized several research areas in computer vision and medical imaging. Several DNN-based methods have been developed to predict E-field maps and reduce the prediction time using a powerful graphical computation unit (GPU). Figure 3 provides an overview of three representative DNN-based E-field modeling methods based on [45–47]. Below, these methods are categorized into supervised and self-supervised learning methods. DNN models have also been used to directly predict quantitative measures derived from the E-field, such as maximum E-field intensity and stimulated volume [19], which will not be discussed in this section.

2.3.1 Supervised learning approach

The DNN approach was first used in [45] to predict TMS-induced E-field maps using MRI data. As illustrated in Fig. 3a, this approach takes subject-specific T1w MRI as the input to predict the E-field in a three-dimensional volume. The DNN model is developed based on the standard U-Net architecture [56]. The input and output data array size is $72 \times 144 \times 24$ with 1-mm isotropic voxels (i.e., the magnitude of E-field). The input volume is sampled in a coil-centered coordinate system to adjust for varying coil positions

Fig. 3 Schematic diagrams of the three DNN-based methods for E-Field mapping. The vector fields (i.e., $\frac{\partial A}{\partial t}$ and E) indicate its magnitude
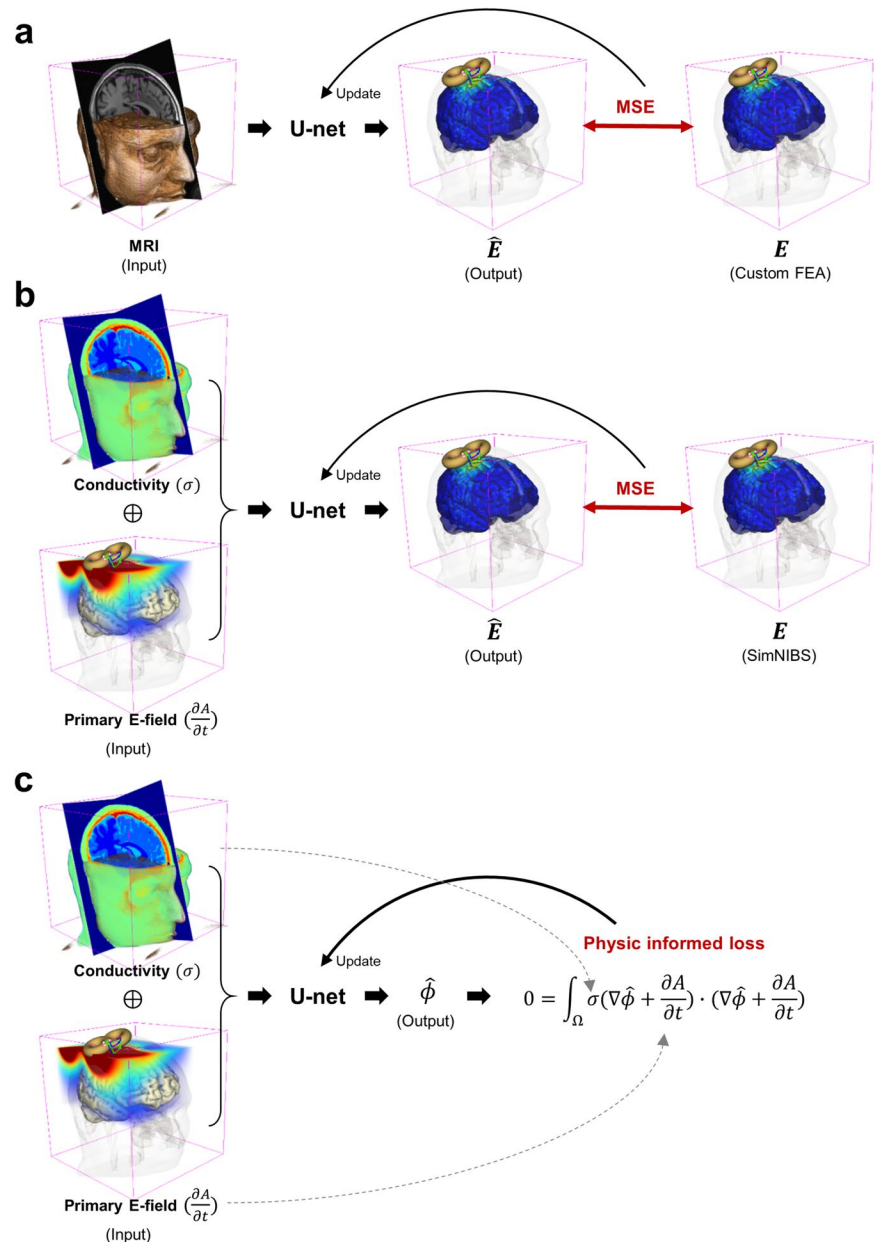
and orientations. The network was trained to minimize the mean squared error (MSE) with reference data generated by a FEM algorithm developed in [57].

The network was trained based on 225,792 samples generated using simulated data from 32 subjects and tested on 35,280 samples from 5 subjects. The evaluation results show that the correlation coefficient between the DNN predicted and reference E-field maps was 0.979 in the hand knob area. The mean relative absolute deviations(MAD) was about 4.45%, which is similar to that of the MSP approach [42]. With the trained DNN model, the prediction time reduced from 3.034 s per trial based on the method in [57] to 0.024 s based on an NVIDIA GeForce GTX 1080 Ti GPU.

However, a limitation of the approach in [45] is that the DNN model depends on the TMS coils. Separate models need to be trained for different types of coils. To overcome the limitation, [46] improved the DNN approach by adding the primary E-field of coils at different positions and orientations together with MRI-based conductivity maps as the input to predict vector E-field maps, as illustrated in Fig. 3b. Moreover, the network used a modified 3D-ResUNet architecture that integrates the residual module [58] and multi-scale features [59] to improve the prediction accuracy.

Two types of DNN models were trained in [46] based on different types of input images. The first model type was trained using T1w MRI and the primary E-field to predict vector E-field represented by a data array of

$180 \times 220 \times 120 \times 3$ with 1-mm spatial resolution. The second type of input includes the principal eigenvectors of the diffusion tensor imaging (DTI) and the primary E-field. The networks were trained to minimize the MSE compared to reference data computed using SimNIBS [18]. The T1w-based model was trained using 81,120 volumes sampled from 20 subjects. The DTI-based model was trained using a maximum number of 243,360 volumes. Both methods were tested using 20,280 volumes of samples from 5 independent subjects.

The DNN models were evaluated in brain surface and volume space in [46] with the more reliable performance shown by the surface-based evaluations. The T1w-MRI-based model showed a correlation coefficient = 0.986, mean relative error (MRE) = 15.2%, and the distance (Dist) between the position of E-field peak vertices is Dist = 3.73 mm. We note that the MRE is defined as

$$\text{MRE} = \frac{1}{N_{\text{vox}}} \sum_{k=1}^{N_{\text{vox}}} \frac{|E_{\text{ref}}(v_i) - E_{\text{pred}}(v_i)|}{E_{\text{ref}}(v_i)}, \tag{18}$$

which is sensitive to estimation errors in brain regions with lower intensity. Therefore, RE or RME are more relevant metrics for determining the estimation error for dosimetry analysis.

The DTI-based model showed a CC = 0.997, MRE = 0.077, and Dist = 1.3 mm. Once the neural network is trained, the prediction speed is about 0.24 s per coil position using an NVIDIA TITAN RTX GPU. Of note, the DNN models were trained using a Fig. 8 coil and showed accurate prediction for a circular coil, which indicated that the DNN learning meaningful maps between the input and output data.

2.3.2 Self-supervised approach

Figure 3 illustrates the self-supervised DNN approach in [47]. Unlike prior studies, the focus shifts to training a neural network for electric potential (ϕ) prediction instead of direct E-field (E) acquisition in the context of [47]. Diverging from approaches relying on pre-trained simulation outcomes, this methodology involves minimizing the energy function Eq. (19) derived from equations Eqs. (2) and (4) to predict electric potential.

$$\mathcal{L}(\theta; \phi_\theta) = \int_\Omega \sigma \left(\nabla \phi_\theta + \frac{\partial A}{\partial t} \right) \cdot \left(\nabla \phi_\theta + \frac{\partial A}{\partial t} \right) dv \tag{19}$$

Subsequently, the calculated ϕ_θ is employed to derive the E_θ through Eq. (2). This approach eliminates the need for precomputed E-fields from FEM or boundary element modeling (BEM) during the model training phase.

The input configuration for this method aligns with [46]'s methodology, featuring a 4D matrix (i.e., $208 \times 288 \times 304 \times 4$) encompassing primary E-field ($\frac{\partial A}{\partial t}$) and an individual head model (i.e., conductivity map). The output maintains a 3D structure mirroring the input domain ($208 \times 288 \times 304$). Leveraging the U-net network architecture, three models are constructed for each target location. The trained network showcases a computation time of approximately 1.4 s on an NVIDIA TITAN RTX GPU with 24G memory. The performance of the self-supervised approach was evaluated using predicted E-field maps with coil placed at different positions within the dorsolateral prefrontal cortex (DLPFC) area with different orientations. Compared with results based on SIMNIBS, the prediction results have RE = 1.2% and CC = 0.98. The prediction error was relatively larger for regions with a high E-field magnitude. For regions with E-field magnitude exceeding 50% of the maximum magnitude, the RME = 5.5%.

3 Real-time E-field visualization software

The standard navigated TMS method uses a neuronavigation system to guide the position of the coil. Therefore, this approach is only feasible for a predefined brain target or coil positions. Advanced neuronavigation systems, such as Brainsight TMS Navigation system (Brainbox Ltd, Cardiff, United Kingdom), can be integrated with SimNIBS to visualize E-field maps computed before the TMS experiment. However, E-field mapping can not be updated in real-time during coil movement because of the long computation time.

The Nexstim TMS system (Nexstim, Helsinki, Finnland) [26] is a commercial product that integrates a multi-sphere based head-model based E-field modeling method with a neuronavigation system to provide real-time E-field navigated TMS. It was shown in [15] that E-field navigated TMS can significantly improve the accuracy localizing of motor cortex for neurosurgery. To further improve TMS targeting, a real-time diffusion MRI tractography algorithm was also developed that can integrated into the neuronavigation system to identify the structural brain network related to the target [25].

3.1 SlicerTMS software

An open-source software, named SlicerTMS [48], was recently developed based on the 3D Slicer [60] to provide a research platform for E-field navigated TMS. 3D Slicer is a widely used open-source software platform for medical image analysis and visualization. It has integrated several advanced functions for image analysis and surgical planning, such as the OpenIGTLink module [61] for integration with

neuronavigation systems and the SlicerDMRI module [62] for diffusion MRI tractography computation and visualization. The diffusion MRI tractography is a technique to estimate the structural connectivity between brain regions based on direction-dependent water diffusion in the white matter [63]. The structural connectivity can provide complementary information to improve the targeting reliability using subjection specificity functional connectivity alone [64]. SlicerTMS uses this module to provide several advanced features for E-field navigated TMS, as illustrated in Fig. 4. First, SlicerTMS uses the OpenIGT tool to stream data between a DNN-based E-field solver and the 3DSlicer graphical user interface (GUI). The E-field solver can be implemented on the same workstation as the GUI or a remote GPU server so that SlicerTMS can still be used in a clinical environment without an on-site GPU machine. Second, E-field maps can be visualized on brain surfaces as in Fig. 4a, dMRI tractography fiber bundles, and volume rendering as shown in Fig. 4b. With the optimized data rendering techniques in 3D Slicer, the data visualization procedures only take 5–10 ms across different computer systems [48]. Third, SlicerTMS can be integrated with a neuronavigation system, as shown in Fig. 4c. A user can freely adjust the coil position using a mouse, manually enter the coil position, or integrate the coil position with a navigation system.

The SlicerTMS software has a general architecture that can be integrated into different types of E-field solvers with navigated TMS. It provides a default E-field solver based on the DNN method in [46]. To further improve the prediction accuracy and prediction speed, the DNN model was trained using data estimated based on eight coils of different shapes, including 4 Fig. 8 coils, three circular coils, and 1 H1 coil based on the vector potential profile provided by [65]. The training data was computed using SimNIBS3.2 [18] using MRI data from 60 subjects from the Human Connectome Project (HCP) [66]. To enhance prediction speed, the simulated data was sampled from mesh data to volume space using *msh2nii* to a data matrix of size $70 \times 90 \times 50$ with $2 \times 2 \times 2$ mm^2 isotropic voxels. Each coil was applied to simulate E-field for 20 randomly chosen subsets of subjects at 34 positions as coil centers and six random coil orientations, resulting in 32,640 total training volumes. The performance was tested in 5880 E-field volumes, including 2476 volumes based on a Fig. 8 coil (Magstim 25-mm Fig. 8), 2476 volumes based on a circular coil (Magstim, 70-mm circular), and 928 H1 coil (Brainsway). The training approach and the DNN architecture were the same as the approach in [46].

The left three columns of Fig. 5 show the comparison of reference and DNN-predicted E-field sampled on the mid-thickness layer of the brain of three subjects using three types of coils, respectively. The DNN method takes about 15 ms to predict the E-field at each coil position, which is significantly faster than the reference method (> 10 s), and the method in [46] is based on a larger matrix size and higher spatial resolution. The last column of Fig. 5 shows the averaged evaluation metrics for the coils overall testing detests. The RME measure based on the 100 highest E-field values was lower than 5% for all three coils. Moreover, the distance between the peak locations of the reference and DNN-predicted E-field maps for the three coils were 0.39 mm, 1.05 mm and 2.11 mm, respectively.

4 Discussion and conclusion

This paper has reviewed several real-time or near-real-time TMS E-field prediction techniques. A summary of the algorithms is provided in Table 1. In addition to the fast-BEM method, modern fast E-field prediction algorithms can be classified into two groups, including methods using basis representations and deep neural networks. The basis-representation methods use a linear combination of a fixed set of E-field maps to represent the total E-field of a moving coil. The MSP method [42] uses the basis matrices based on the total E-field of dipoles placed at a large set of positions around the head and uses the regularized minimum norm method to estimate the representation coefficients. Overall, the RME error was around 5% for different coil positions.

Fig. 4 Illustration of the graphical user interface (GUI) of the SlicerTMS software (**a**), advanced visualization techniques (**b**), and integration with the neuronavigation system (**c**)
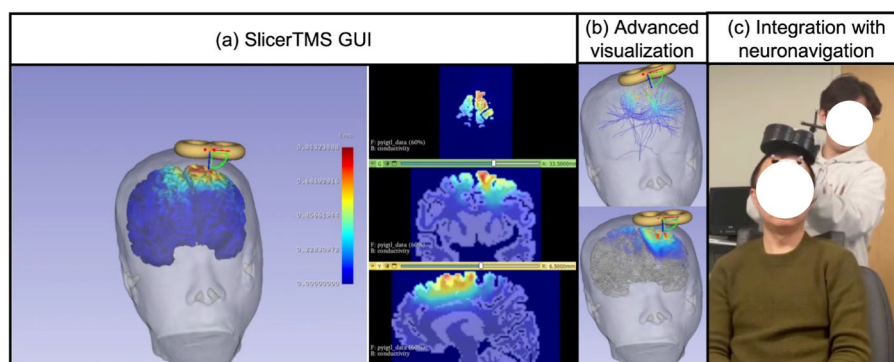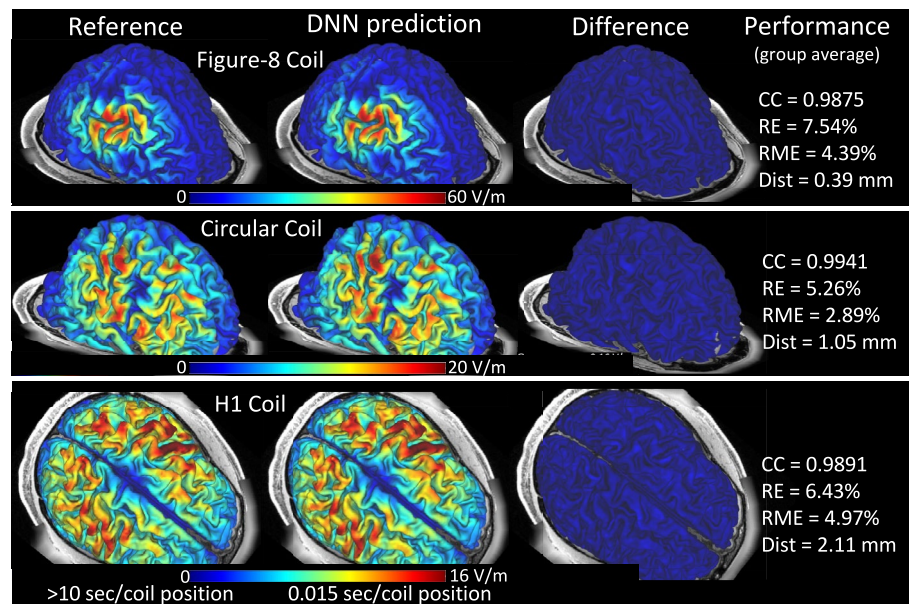
Fig. 5 An illustration of the performance of the DNN model included in SlicerTMS for three types of coils

The ACA–ADM [43] and PMD [44] methods use low-rank approximation techniques to improve the time efficiency for dictionary learning. These methods use the ADM method [55] to reduce the computation time for a small ROI. The improved time efficiency makes it possible to significantly increase the number of basis functions to reduce the prediction error to about 2%. The orthonormal basis function method [44] uses the low-rank matrix approximation technique similar to the PMD method [44] but with an analytical solution for the representation coefficients that significantly reduces the computation time to less than 2.5 ms per coil position in a GPU.

The DNN methods provide an alternative solution for (near) real-time E-field prediction. The supervised learning approach has shown that the trained neural network can predict whole-brain E-field for individual subjects without additional training. The method in [46] showed that the mean relative error of whole-brain is about 15%, which was driven by estimation error in brain regions with lower intensity. A new version of the network model (including the eigenvector from the conductivity tensor) was trained in this work using the same method as in [46] and evaluated using standard metrics. The results show that the whole-brain relative error is about 5–7% similar to the error reported in [45], and the relative error around the peak region is lower than 5% across different coils. However, these models have the limitation that their accuracy depends on existing simulation results as they are trained based on them.

The self-learning method [47], which uses DNN to numerically solve the underlying governing equations, eliminates the need for pre-calculated training data and provides a significantly lower prediction error of about 1.2% in peak values. However, this approach requires the entire high-resolution head model to compute the boundary conditions, which significantly increases the computation time to about 1.4 s. Moreover, the DNN model must be trained separately for different brain regions, as reported in [47].

A major advantage of the basis-representation techniques compared to DNN-based methods is that the former methods provide faster computation time, which can be as low as 2.5 ms, and higher accuracy of 2% error. However, a major limitation of the basis-representation techniques is that they require a very long pre-processing time (> 10 h) to learn the basis matrices for individual subjects. These methods also require an additional few hours to create head mesh models. On the other hand, the DNN methods have shown better generalizability since a trained model can be applied to different subjects and coils. A whole-brain E-field with 315,000 voxels can be predicted using a DNN model in 15 ms in a GPU. However, a limitation of the DNN method is that the prediction accuracy (RME: 3–5%, RE: 5–7.5%) is relatively lower than basis-representation methods. Therefore, future works are needed to enhance the prediction accuracy of the DNN models. Since the self-learning technique has shown enhanced prediction accuracy, a promising future direction is to integrate the physical constraints with DNN models using, for example, the physics-informed neural networks (PINN) to increase the prediction accuracy further.

This paper also reviewed an open-source software, SlicerTMS, that has shown real-time navigated E-field prediction is feasible for TMS treatment. The predicted E-field maps have much higher resolution than that provided by the commercial software. Moreover, SlicerTMS provides different visualization techniques to illustrate the E-field on the brain surface and probe the dMRI tractography fiber bundles related to the stimulated brain regions by a moving coil. The

architecture of SlicerTMS is flexible to integrate different E-field solvers into the navigation and visualization tools. Currently, the software integrates the DNN model developed in [46]. Future work is needed to integrate other real-time E-field modeling algorithms so that users can cross-validate the prediction results for more reliable target selection. Moreover, it will be helpful to integrate quantitative E-field outcome measures. TMS has been used as a noninvasive tool to localize brain functional regions for surgical planning [17], including cortical areas related to motor and language functions [15, 16]. While the peak coordinate or peak volume of the E-field is usually used to guide the localization of the brain target [15, 16, 67], other measures such as the center of gravity of multiple E-field maps may provide more reliable targeting [68]. Thus, providing reliable E-field-based measures is critical to improving the accuracy of localizing brain areas [69]. There is software named TMSmap developed for computing different types of E-field measures to improve targeting [70]. Integrating these measures with navigated real-time prediction software will be useful to streamline the application of the E-field guided targeting in TMS.

In summary, recent computation algorithms and software tools developments make real-time E-field prediction feasible in TMS experiments. The integration of real-time E-field measures with TMS targeting and dosimetry can significantly enhance the treatment efficacy for brain diseases.

Declarations

Competing interests The authors have no relevant financial or non-financial interests to disclose

Consent to publish The authors affirm that human research participants provided informed consent for publications of Fig. 4

Ethical approval The MRI data was acquired with approval from the Institutional Review Boards (IRBs) of Brigham and Women's Hospital with a signed consent form from the subject. The E-field modeling experiment in Fig. 4 was an observational study without any stimulation pulses applied. The Research Ethics Committee has confirmed that no ethical approval is required.

References

1. Barker AT, Jalinous R, Freeston IL. Non-invasive magnetic stimulation of human motor cortex. Lancet. 1985;325:1106–7.
2. Hallett M. Transcranial magnetic stimulation and the human brain. Nature. 2000;406:147–50.
3. George MS, Nahas Z, Lisanby SH, Schlaepfer T, Kozel F, Greenberg BD. Transcranial magnetic stimulation. Neurosurg Clin N Am. 2003;14:283–301.
4. O'Reardon JP, Solvason HB, Janicak PG, Sampson S, Isenberg KE, Nahas Z, McDonald WM, Avery D, Fitzgerald PB, Loo C, Demitrack MA, George MS, Sackeim HA. Efficacy and safety of transcranial magnetic stimulation in the acute treatment of major depression: a multisite randomized controlled trial. Biol Psychiatry. 2007;62:1208–16.
5. Mantovani A, Simpson HB, Fallon BA, Rossi S, Lisanby SH. Randomized sham-controlled trial of repetitive transcranial magnetic stimulation in treatment-resistant obsessive-compulsive disorder. Int J Neuropsychopharmacol. 2010;13:217.
6. Lipton RB, Dodick DW, Silberstein SD, Saper JR, Aurora SK, Pearlman SH, Fischell RE, Ruppel PL, Goadsby PJ. Single-pulse transcranial magnetic stimulation for acute treatment of migraine with aura: a randomised, double-blind, parallel-group, sham-controlled trial. Lancet Neurol. 2010;9:373–80.
7. Zangen A, Moshe H, Martinez D, Barnea-Ygael N, Vapnik T, Bystritsky A, Duffy W, Toder D, Casuto L, Grosz ML, Nunes EV, Ward H, Tendler A, Feifel D, Morales O, Roth Y, Iosifescu D, Winston J, Wirecki T, Stein A, Deutsch F, Li X, George MS. Repetitive transcranial magnetic stimulation for smoking cessation: a pivotal multicenter double-blind randomized controlled trial. World Psychiatry. 2021;20:397–404.
8. Deng Z-D, Luber B, Balderston NL, Velez-Afanador M, Noh MM, Thomas J, Altekruse WC, Exley SL, Awasthi S, Lisanby SH. Device-based modulation of neurocircuits as a therapeutic for psychiatric disorders. Annu Rev Pharmacol Toxicol. 2020;60:591–614.
9. Fox MD, Buckner RL, White MP, Greicius MD, Pascual-Leone A. Efficacy of transcranial magnetic stimulation targets for depression is related to intrinsic functional connectivity with the subgenual cingulate. Biol Psychiatry. 2012;72:595–603.
10. Fox MD, Liu H, Pascual-Leone A. Identification of reproducible individualized targets for treatment of depression with TMS based on intrinsic connectivity. Neuroimage. 2013;66:151–60.
11. Opitz A, Fox MD, Craddock RC, Colcombe S, Milham MP. An integrated framework for targeting functional networks via transcranial magnetic stimulation. Neuroimage. 2016;127:86–96.
12. Klooster DC, Vos IN, Caeyenberghs K, Leemans A, David S, Besseling RM, Aldenkamp AP, Baeken C. Indirect frontocingulate structural connectivity predicts clinical response to accelerated rTMS in major depressive disorder. J Psychiatry Neurosci. 2020;45:243–52.
13. Luber B, Davis SW, Deng Z-D, Murphy D, Martella A, Peterchev AV, Lisanby SH. Using diffusion tensor imaging to effectively target TMS to deep brain structures. Neuroimage. 2022;249: 118863.
14. Ning L, Rathi Y, Barbour T, Makris N, Camprodon JA. White matter markers and predictors for subject-specific rTMS response in major depressive disorder. J Affect Disord. 2022;299:207–14.
15. Sollmann N, Goblirsch-Kolb MF, Ille S, Butenschoen VM, Boeckh-Behrens T, Meyer B, Ringel F, Krieg SM. Comparison between electric-field-navigated and line-navigated TMS for cortical motor mapping in patients with brain tumors. Acta Neurochir. 2016;158:2277–89.
16. Bährend I, Muench MR, Schneider H, Moshourab R, Dreyer FR, Vajkoczy P, Picht T, Faust K. Incidence and linguistic quality of speech errors: a comparison of preoperative transcranial magnetic

stimulation and intraoperative direct cortex stimulation. J Neurosurg. 2020;134:1409–18.

17. Haddad AF, Young JS, Berger MS, Tarapore PE. Preoperative applications of navigated transcranial magnetic stimulation. Front Neurol. 2021;11: 628903.

18. Saturnino GB, Puonti O, Nielsen JD, Antonenko D, Madsen KH, Thielscher A. SimNIBS 2.1: A Comprehensive Pipeline for Individualized Electric Field Modelling for Transcranial Brain Stimulation. In: Makarov S, Horner M, Noetscher G (eds) Brain and human body modeling: computational human modeling at EMBC 2018. Springer, Cham; 2019.

19. Afuwape OF, Rastogi P, Jiles D. Effect of coil positioning and orientation of the quadruple butterfly coil during transcranial magnetic stimulation. AIP Adv. 2021;11: 015212.

20. Silva S, Basser PJ, Miranda PC. Elucidating the mechanisms and loci of neuronal excitation by transcranial magnetic stimulation using a finite element model of a cortical sulcus. Clin Neurophysiol. 2008;119:2405–13.

21. Makarov SN, Wartman WA, Daneshzand M, Fujimoto K, Raij T, Nummenmaa A. A software toolkit for TMS electric-field modeling with boundary element fast multipole method: an efficient MATLAB implementation. J Neural Eng. 2020;17: 046023.

22. Caulfield KA, Li X, George MS. Four electric field modeling methods of dosing prefrontal transcranial magnetic stimulation (TMS): introducing APEX MT dosimetry. Brain Stimul. 2021;14:1032–4.

23. Nummenmaa A, McNab JA, Savadjiev P, Okada Y, Hämäläinen MS, Wang R, Wald LL, Pascual-Leone A, Wedeen VJ, Raij T. Targeting of white matter tracts with transcranial magnetic stimulation. Brain Stimul. 2014;7(1):80–4.

24. Puonti O, Van Leemput K, Saturnino GB, Siebner HR, Madsen KH, Thielscher A. Accurate and robust whole-head segmentation from magnetic resonance images for individualized head modeling. Neuroimage. 2020;219: 117044.

25. Aydogan DB, Souza VH, Lioumis P, Ilmoniemi RJ. Towards real-time tractography-based TMS neuronavigation. Brain Stimul. 2021;14:1609.

26. Hannula H, Ilmoniemi RJ. Basic principles of navigated TMS. In: Krieg SM (eds) Navigated transcranial magnetic stimulation in neurosurgery. Springer International Publishing, Cham; 2017. pp. 3–29.

27. Ruohonen J, Ilmoniemi RJ. Modeling of the stimulating field generation in TMS. Electroencephalogr Clin Neurophysiol Suppl. 1999;51:30–40.

28. Bungert A, Antunes A, Espenhahn S, Thielscher A. Where does TMS stimulate the motor cortex? Combining electrophysiological measurements and realistic field estimates to reveal the affected cortex position. Cereb Cortex. 2017;27:5083–94.

29. Laakso I, Murakami T, Hirata A, Ugawa Y. Where and what TMS activates: experiments and modeling. Brain Stimul. 2018;11:166–74.

30. Makarov SN, Noetscher GM, Raij T, Nummenmaa A. A quasi-static boundary element approach with fast multipole acceleration for high-resolution bioelectromagnetic models. IEEE Trans Biomed Eng. 2018;65:2675–83.

31. Htet AT, Saturnino GB, Burnham EH, Noetscher GM, Nummenmaa A, Makarov SN. Comparative performance of the finite element method and the boundary element fast multipole method for problems mimicking transcranial magnetic stimulation (TMS). J Neural Eng. 2019;16: 024001.

32. Makaroff SN, Qi Z, Rachh M, Wartman WA, Weise K, Noetscher GM, Daneshzand M, Deng Z-D, Greengard L, Nummenmaa AR. A fast direct solver for surface-based whole-head modeling of transcranial magnetic stimulation. Sci Rep. 2023;13:18657.

33. Toschi N, Welt T, Guerrisi M, Keck ME. A reconstruction of the conductive phenomena elicited by transcranial magnetic stimulation in heterogeneous brain tissue. Physica Med. 2008;24:80–6.

34. Paffi A, Camera F, Carducci F, Rubino G, Tampieri P, Liberti M, Apollonio F. A Computational model for real-time calculation of electric field due to transcranial magnetic stimulation in clinics. Int J Antennas Propag. 2015;2015: e976854.

35. Pérez-Benítez JA, Martínez-Ortiz P, Aguila-Muñoz J. A review of formulations, boundary value problems and solutions for numerical computation of transcranial magnetic stimulation fields. Brain Sci. 2023;13:1142.

36. Roth BJ, Saypol JM, Hallett M, Cohen LG. A theoretical calculation of the electric field induced in the cortex during magnetic stimulation. Electroencephalogr Clin Neurophysiol Evoked Potentials Sect. 1991;81:47–56.

37. Davey K, Cheng C, Epstein C. Prediction of magnetically induced electric fields in biological tissue. IEEE Trans Biomed Eng. 1991;38:418–22.

38. Güllmar D, Haueisen J, Reichenbach JR. Influence of anisotropic electrical conductivity in white matter tissue on the EEG/MEG forward and inverse solution. A high-resolution whole head simulation study. Neuroimage. 2010;51:145–63.

39. Gomez LJ, Dannhauer M, Koponen LM, Peterchev AV. Conditions for numerically accurate TMS electric field simulation. Brain Stimul. 2020;13:157–66.

40. Stenroos M, Koponen LM. Real-time computation of the TMS-induced electric field in a realistic head model. Neuroimage. 2019;203: 116159.

41. Hasan NI, Dannhauer M, Wang D, Deng Z-D, Gomez LJ. Real-time computation of brain E-field for enhanced transcranial magnetic stimulation neuronavigation and optimization. Bioengineering. 2023.

42. Daneshzand M, Makarov SN, De Lara LIN, Guerin B, McNab J, Rosen BR, Hämäläinen MS, Raij T, Nummenmaa A. Rapid computation of TMS-induced E-fields using a dipole-based magnetic stimulation profile approach. Neuroimage. 2021;237: 118097.

43. Wang D, Hasan NI, Dannhauer M, Yucel AC, Gomez LJ. Fast computational E-field dosimetry for transcranial magnetic stimulation using adaptive cross approximation and auxiliary dipole method (ACA-ADM). Neuroimage. 2023;267: 119850.

44. Hasan NI, Wang D, Gomez LJ. Fast and accurate computational E-field dosimetry for group-level transcranial magnetic stimulation targeting. Comput Biol Med. 2023;167: 107614.

45. Yokota T, Maki T, Nagata T, Murakami T, Ugawa Y, Laakso I, Hirata A, Hontani H. Real-time estimation of electric fields induced by transcranial magnetic stimulation with deep neural networks. Brain Stimul. 2019;12:1500–7.

46. Xu G, Rathi Y, Camprodon JA, Cao H, Ning L. Rapid whole-brain electric field mapping in transcranial magnetic stimulation using deep learning. PLoS ONE. 2021;16: e0254588.

47. Li H, Deng Z-D, Oathes D, Fan Y. Computation of transcranial magnetic stimulation electric fields using self-supervised deep learning. Neuroimage. 2022;264: 119705.

48. Franke L, Park TY, Luo J, Rathi Y, Pieper S, Ning L, Haehn D. SlicerTMS: Interactive real-time visualization of transcranial magnetic stimulation using augmented reality and deep learning. 2023. arXiv:2305.06459 [cs, eess, q-bio].

49. Gomez LJ, Goetz SM, Peterchev AV. Design of transcranial magnetic stimulation coils with optimal trade-off between depth, focality, and energy. J Neural Eng. 2018;15: 046033.

50. Koponen LM, Nieminen JO, Mutanen TP, Stenroos M, Ilmoniemi RJ. Coil optimisation for transcranial magnetic stimulation in realistic head geometry. Brain Stimul. 2017;10:795–805.

51. Bebendorf M, Rjasanow S. Adaptive low-rank approximation of collocation matrices. Computing. 2003;70:1–24.

52. Bebendorf M. Adaptive cross approximation of multivariate functions. Constr Approx. 2011;34:149–79.

53. Zhao K, Vouvakis M, Lee J-F. The adaptive cross approximation algorithm for accelerated method of moments computations of EMC problems. IEEE Trans Electromagn Compat. 2005;47:763–73.

54. Trefethen LN, Bau D. Numerical linear algebra. Philadelphia: Society for Industrial and Applied Mathematics; 1997.

55. Gomez LJ, Dannhauer M, Peterchev AV. Fast computational optimization of TMS coil placement for individualized electric field targeting. Neuroimage. 2021;228: 117696.

56. Ronneberger O, Fischer P, Brox T. U-Net: convolutional networks for biomedical image segmentation. In: Navab N, Hornegger J, Wells WM, Frangi AF (eds) Medical image computing and computer-assisted intervention—MICCAI 2015, Lecture Notes in Computer Science. Springer International Publishing, Cham; 2015. pp. 234–241.

57. Laakso I, Hirata A. Fast multigrid-based computation of the induced electric field for transcranial magnetic stimulation. Phys Med Biol. 2012;57:7753–65.

58. He K, Zhang X, Ren S, Sun J. Deep residual learning for image recognition. In: 2016 IEEE conference on computer vision and pattern recognition (CVPR). IEEE, Las Vegas; 2016. pp. 770–778.

59. Zeng G, Yang X, Li J, Yu L, Heng P-A, Zheng G. 3D U-net with multi-level deep supervision: fully automatic segmentation of proximal femur in 3D MR images. In: Wang Q, Shi Y, Suk H-I, Suzuki K (eds) Machine learning in medical imaging, lecture notes in computer science, vol. 10541. Springer International Publishing, Cham; 2017. pp. 274–282.

60. Kikinis R, Pieper SD, Vosburgh KG. 3D slicer: a platform for subject-specific image analysis, visualization, and clinical support. In: Jolesz FA (eds) Intraoperative imaging and image-guided therapy. Springer, New York; 2014. pp. 277–289.

61. Tokuda J, Fischer GS, Papademetris X, Yaniv X, Ibanez L, Cheng P, Liu H, Blevins J, Arata J, Golby AJ, Kapur T, Pieper S, Burdette EC, Fichtinger G, Tempany CM, Hata N. OpenIGTLink: an open network protocol for image-guided therapy environment. Int J Med Robot Comput Assist Surg. 2009;5(4):423–34. https://doi.org/10.1002/rcs.274.

62. Zhang F, Noh T, Juvekar P, Frisken SF, Rigolo L, Norton I, Kapur T, Pujol S, Wells W, Yarmarkovich A, Kindlmann G, Wassermann D, San Jose Estepar R, Rathi Y, Kikinis R, Johnson HJ, Westin C-F, Pieper S, Golby AJ, O'Donnell LJ. SlicerDMRI: diffusion MRI and tractography research software for brain cancer surgery planning and visualization. JCO Clin Cancer Inform. 2020;4:299–309.

63. Jeurissen B, Descoteaux M, Mori S, Leemans A. Diffusion MRI fiber tractography of the brain. NMR Biomed. 2019;32: e3785.

64. Ning L, Makris N, Camprodon JA, Rathi Y. Limits and reproducibility of resting-state functional MRI definition of DLPFC targets for neuromodulation. Brain Stimul. 2019;12:129–38.

65. Deng Z-D, Lisanby SH, Peterchev AV. Electric field depth-focality tradeoff in transcranial magnetic stimulation: simulation comparison of 50 coil designs. Brain Stimul. 2013;6:1–13.

66. Van Essen DC, Smith SM, Barch DM, Behrens TEJ, Yacoub E, Ugurbil K. WU-Minn HCP consortium, The WU-Minn Human Connectome Project: an overview. NeuroImage 2013;80:62–79.

67. Lee EG, Rastogi P, Hadimani RL, Jiles DC, Camprodon JA. Impact of non-brain anatomy and coil orientation on inter- and intra-subject variability in TMS at midline. Clin Neurophysiol. 2018;129:1873–83.

68. Opitz A, Legon W, Rowlands A, Bickel WK, Paulus W, Tyler WJ. Physiological observations validate finite element models for estimating subject-specific electric field distributions induced by transcranial magnetic stimulation of the human motor cortex. Neuroimage. 2013;81:253–64.

69. Van Hoornweder S, Nuyts M, Frieske J, Verstraelen S, Meesen RLJ, Caulfield KA. Outcome measures for electric field modeling in tES and TMS: a systematic review and large-scale modeling study. Neuroimage. 2023;281: 120379.

70. Novikov PA, Nazarova MA, Nikulin VV. TMSmap—software for quantitative analysis of TMS mapping results. Front Hum Neurosci. 2018;12:239.